DENTAL MATERIALS 34 (2018) 1041–1053

Available online at www.sciencedirect.com

ScienceDirect

journal homepage: www.intl.elsevierhealth.com/journals/dema

Effect of hydration and crack orientation on crack-tip strain, crack opening displacement and crack-tip shielding in elephant dentin

Xuekun Lu[a,b], *Shelley D. Rawson*[a], *Philip J. Withers*[a,*]

[a] *School of Materials, University of Manchester, Manchester M13 9PL, UK*
[b] *Electrochemical Innovation Lab, Department of Chemical Engineering, University College London, London WC1E 7JE, UK*

ARTICLE INFO

Article history:
Received 1 October 2017
Received in revised form
11 March 2018
Accepted 4 April 2018

Keywords:
Ivory
Moisture
Crack-tip plasticity
Intrinsic and extrinsic toughening
Strain
Bridging
Finger crack

ABSTRACT

Objectives. To quantify the extent of crack-tip plasticity, crack opening displacement (COD) and crack bridging for crack growth perpendicular (HAH) and parallel (RAR) to the tubules in elephant dentin under both hydrated and dry conditions to better understand their influence on intrinsic and extrinsic toughening during crack growth.

Methods. Compact tension test-pieces were prepared from a tusk of African elephant ivory. Crack-tip strain mapping and COD measurements by digital image correlation (DIC) technique were made under incremental loading and unloading of cracks for hydrated and dry dentin of different orientations.

Results. For the RAR test-piece the plastic zones were significantly larger in the hydrated condition compared to when dry. By contrast, the plastic strains in the HAH test-piece were negligible in both wet and dry conditions. In the RAR condition the crack front was broken up into overlapping longitudinal 'fingers' with crack bridging regions in between, the ligaments extending 400 μm behind the crack front in the dry case. This could only be seen in 3D by X-ray CT. Extrinsic shielding reduces the crack-tip stresses by 52% and 40% for hydrated and dry RAR test-pieces respectively. No significant bridging was found in the HAH case.

Significance. For crack growth parallel to the tubules, collagen plasticity determines the intrinsic toughening, whereas microcracking from the tubules governs extrinsic shielding via ligament bridging, which is maintained further behind the crack in the hydrated case. For cracks grown perpendicular to the tubules, neither toughening mechanisms are significant.

1. Introduction

The crack-resistance of dentin, as the major constituent of teeth and tusk, is a subject of considerable biomechanical interest. The resistance of a material to crack propagation (its fracture toughness) is related to intrinsic and extrinsic toughening mechanisms. Extrinsic toughening mechanisms operate primarily behind the crack tip by introducing crack-tip shielding, which reduces the local stress intensity actually

* *Corresponding author.*
E-mail address: p.j.withers@manchester.ac.uk (P.J. Withers).
https://doi.org/10.1016/j.dental.2018.04.002

experienced at the crack tip. Intrinsic toughening mechanisms operate ahead of the crack tip and contribute to the material's inherent resistance to crack growth [1].

This paper aims to characterize and compare the extent of crack-tip plasticity (intrinsic toughening) and bridging (extrinsic toughing) of elephant dentin under hydrated and dry conditions to reveal the importance of the microstructure in inhibiting crack propagation. From a practical viewpoint, elephant dentin (tusk) has the advantage over human dentin that tusks are very much larger than human teeth making the preparation of nominally identical compact tension test-pieces of different orientations from the same region easier than for human teeth [2] where sample to sample variations would increase the scatter. Ivory tusk is made up of a peripheral component, the cementum, continuous with, but structurally different from, enamel and a main core comprising dentin (see Fig. 1a). The cementum layer is softer than the dentin inside [3]. The dentinal tubules, are the predominant feature in the main dentin, running approximately radially from the central pulp to the periphery of the dentin (see Fig. 1b). These tubules are embedded in a mineralized collagen matrix, which consists of Type I collagen fibrils and Mg-containing hydroxyapatite [3–8]: the highly mineralized hydroxyapatite (HAP) improves the stiffness, while collagen provides toughness [9]. While the main constituents of elephant and human dentin are similar, there are some important differences. Firstly, while human dentin has tubules of approximately circular cross-section, the tubules in elephant dentin are elliptical with the major axis parallel to the length of the tusk (see Fig. 1c and f). This ellipticity is often exaggerated further in micrographs because the tubules also have a periodic wavy trajectory as they emanate radially from the central pulp cavity of the tusk to the cementum layer [10]. Moreover, elephant dentin has no highly mineralized peritubular cuff. Another critical difference is that in human dentin the collagen fibrils are arranged in a planar random mat, perpendicular to the long axis of the tubules [11]. As such they form a mesh and cross-link around the tubules to provide its desirable mechanical properties [8,12]. By contrast recent work by Alberic [13] and Lu [14] suggest that for elephant dentin the collagen fibrils are approximately aligned (+/−10°) to the semi major axis of the tubules, which coincides with the axial direction of the tusk (see Fig. 1e and f).

In recent years, much work has been done on the fracture mechanics of human, bovine and elephant dentin [15–18]. Crack growth is highly anisotropic. For most kinds of dentin (e.g. human, bovine and elephant dentin), the fracture toughness K_c is 55–65% higher for cracks propagating parallel to the long axis of the dentinal tubules compared to crack propagation perpendicular to the tubules [2,17,19,20] and the fatigue life in human dentin is two orders of magnitude longer for cracks growing parallel to the tubules as opposed to perpendicular to them [4,21]. Moreover, it has been found that fracture toughness increases with the hydration level [22] and tends to fall with the age of the donor [23,24]. Several toughening mechanisms in dentin, particularly for the case where a crack propagates parallel to the tubules, have been proposed such as crack blunting [2,24], crack-tip bridging [2,19,24,25], and microcracking [19,25].

The resistance-curve (R-curve) is a means of evaluating the build-up of crack retarding effects during subcritical crack propagation (i.e. before unstable fracture occurs). Rising R-curve behavior is particularly important in biomaterials, e.g. teeth, bones and tendons [26–31]. Normally an R-curve is expressed in terms of the crack-driving force (the stress intensity K) as a function of the crack extension, Δa, to quantify the increasing fracture resistance with crack length. Previous investigations have revealed that dentin exhibits much higher fracture toughness and crack growth resistance (expressed via an R-curve) when hydrated rather than dry along with enhanced crack-tip blunting [23,32,33]. Hydration has been reported to decrease the elastic Young's modulus and hardness by approximately 35% and 30% compared with the dry dentin [34–36]. The hydrated tissues exhibit viscoelasticity, demonstrating a good ability to recover the elastic energy stored in the region surrounding the deformed area [37].

Our objective is to quantify the mechanisms of toughening as a function of sample orientation and hydration specifically for elephant dentin. We consider the plastic zone ahead of the crack (intrinsic component) and the extent of crack-tip shielding in the crack wake expressed as the fraction of the applied stress intensity transmitted to the crack tip (extrinsic toughening). Here digital image correlation (DIC) is adopted for full-field crack-tip strain field mapping. It requires no, or very little, sample preparation and can be applied to awkward biological materials. Previously it has been used to quantify volume shrinkage and load transfer in dentin [38,39] and bones [40,41]. Here, it is used for the first time to quantify the elastic and plastic (inelastic) crack-tip strains accumulated as the load is increased for test-pieces cracked in different orientations under both wet and dry condition. The obtained plastic strain sizes are then compared with predictions made using the measured elastic stress fields with different crack-tip yield criteria to establish the crack-tip shielding.

2. Materials and experimental methods

2.1. *Test-piece preparation*

The mature African elephant tusk used in this study originated from Zaire and was impounded at London Heathrow airport and made available by the UK Customs House, ethically and legally, solely for the purpose of scientific research. The hierarchical microstructure of the elephant dentin is illustrated in Fig. 1. Compact tension test-pieces (10 × 8 × 2 mm) conforming to plane strain conditions were prepared based on ASTM E1820 [42]. The test-pieces were extracted from the interior of the elephant ivory sample as shown in (Fig. 1a). In order to investigate the anisotropic properties, two orientations of compact tension test (CT)-pieces were excised: (1) HAH, in which crack plane is in the hoop-axial plane and grows in the hoop direction (Fig. 1f), and (2) RAR, in which the crack plane is in the radial-axial plane and grows in the radial direction (Fig. 1e). The 3D alignment of the dentin tubules was observed using an Xradia Versa XRM-500 laboratory X-ray microscope (Fig. 1b). In reality these tubules are not straight but oscillate over a larger length scale. SEM images show the elliptical cross sections of the tubules (Fig. 1c) and the surrounding collagen fibrils are

seen from the fracture surface (Fig. 1d). It is noted that the tubules are filled with carbonated apatite. Approximately parallel collagen fibrils form (hoop–axial) sheets perpendicular to the axis of the tubules, with the fibril orientation varying within +/−10° of the axial direction (i.e. aligned with the semi major axis of the tubules) (Fig. 1f, e) [13,14]. This lamellar composite structure is popular in the bone and dentin family of materials [43–45].

When preparing the test-pieces a 1 cm thick slice was cut from the top of the ivory sample. Subsequently, the plate was cut into rectangular bars and sliced to make CT blanks (10 × 8 × 2 mm). The pieces of the ivory tusk were stored in distilled water at 4 °C (to prevent fungi growth [34,46]) for more than two weeks to keep them hydrated. Distilled water provides a simple, effective way of storing dentin specimens [47,48]. Previous studies have confirmed that the mineral contents of Ca is essentially the same as in fresh dentin and K, Na and P varies less than 15% compared to the control group after 45 days storage in distilled water [49]. Furthermore since it is the water that is largely responsible for plasticizing the collagen, and the collagen cross-linkage is well maintained in distilled water [50], the mechanical properties are not significantly different to those stored in saturated solution [47,48]. A notch was introduced into the mid-plane of the test-pieces using a 0.3 mm thick rotary wheel and sharpened with a razor blade till the radius of the notch tip was equal to, or below, 5 μm. The test-pieces were then pre-cracked to approx. 250 μm on an Instron-3344 machine under displacement control at 1 μm/s. In order to understand the effect of hydration on the mechanical properties, the pre-cracked HAH and RAR test-pieces were tested in both hydrated (i.e. immersed in distilled water since cut, for at least 72 h before test) and dry (i.e. air-drying the test-piece at room temperature 22 °C with 45–52% relative humidity for 72 h before test) conditions.

2.2. *Scanning electron microscopy*

The cracked and fractured surfaces were imaged using a Philips XL30 FEG scanning electron microscope (SEM), in order to correlate the crack propagation behaviour with the microstructure. Prior to imaging, the surfaces were gold coated to reduce charging artefacts. Secondary electron (SE) imaging mode was used at an accelerating voltage of 10 kV with the spot size of 3.0 and working distance between 10 to 13 mm.

2.3. *Strain measurement by digital image correlation*

Digital image correlation (DIC) is a well-established technique used to trace the movement of surface features during the application of loads by continuously taking pictures using a microscope with a camera attached [51,52]. The images were acquired using a DaVis Axiocam connected to a com-

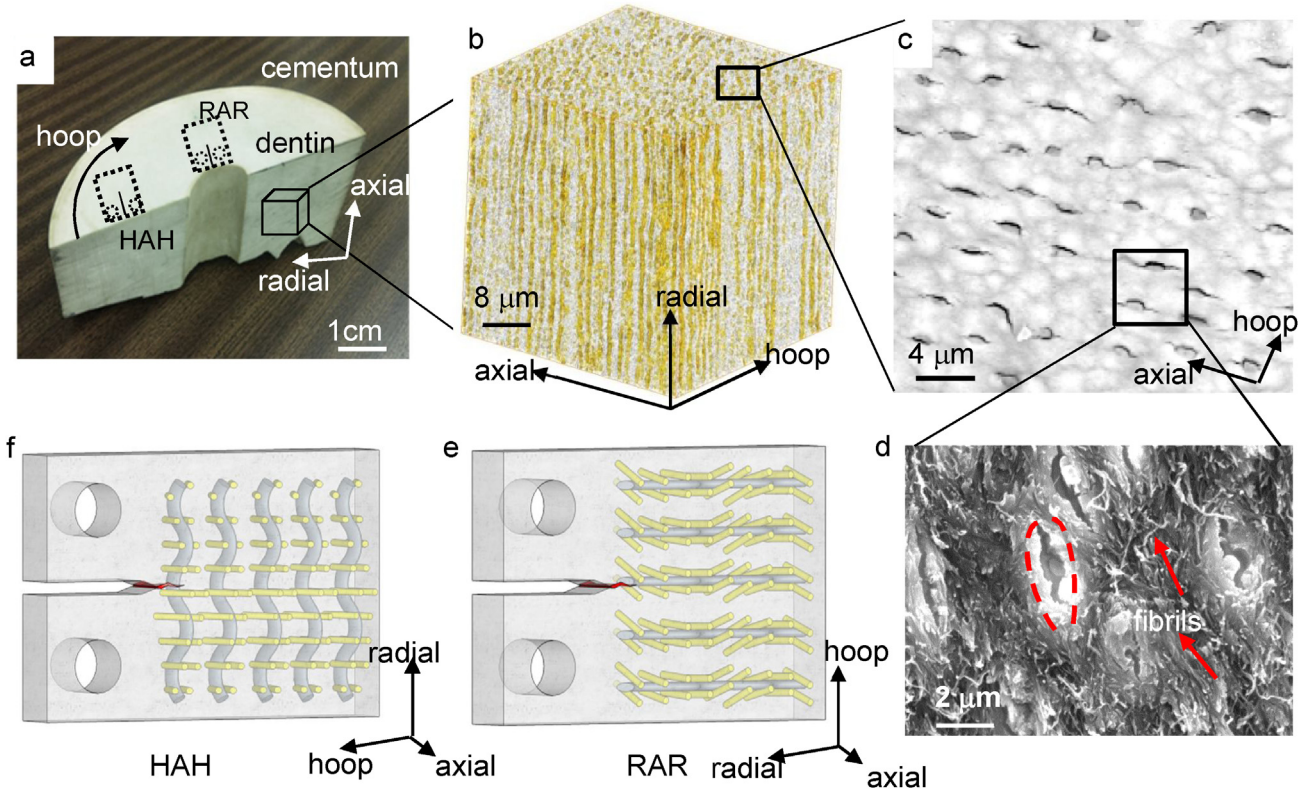

Fig. 1 – The hierarchical structure of elephant dentin microstructure at increasing magnification; (a) photograph of the elephant tusk slice showing the locations of HAH and RAR test-pieces; (b) X-ray CT highlighting the alignment of the tubules; (c) SEM micrograph showing the elliptical cross section of the tubules which is aligned with the axial direction of the tusk along with axial micro-cracks; (d) SEM image showing the micro-cracks along the semi-major axis of the tubules, as well as the approximate alignment of the collagen fibrils; (e) and (f) schematic figures showing the alignment of the tubules (grey) and the arrangement of the collagen fibrils (yellow rods) for the RAR and HAH test-pieces; X-ray CT undertaken on Zeiss Xradia Versa instrument.

puter with LaVision Davis 7.2 software. The object lens of 10× magnification was used giving a resolution of 2.2 μm/pixel. A Kammrath & Weiss GmbH (Germany) microtester with a 500 N load cell (load accuracy approx. 0.1 N and extensometer resolution <100 nm) was used to load and unload the pre-cracked test-pieces at the rate of 2 μm/s and held for 30 s before acquiring images. This dwell time is necessary for system stabilization (i.e. vibration mitigation) and microscope re-focusing, during which time no load drop was observed. The displacements were tracked by DIC over an array of 23 × 26 patches (0.318 × 0.363 mm^2) for HAH, and 25 × 30 patches (0.363 × 0.436 mm^2) for RAR oriented samples. Each patch contained 32 × 32 pixels with 25% overlap between neighboring patches. Measurements were conducted at incremental load cycles (load & unload) until the critical load for both hydrated and dry test-pieces in the different cracking directions. Three test-pieces were measured for each condition with a high degree of reproducibility, such that strain maps from only one sample in each case are presented here.

The uncertainty in the DIC measurements (due to system vibration, variable illumination, microscope drift etc.) was estimated by measuring the displacement on two reference images taken at zero load at an interval of 1 min. The average value of the measured displacement was regarded as the measurement error, which was found to be 0.02 μm for the displacement, corresponding to 0.18% error in strain measurement. To determine the COD the raw images recorded in the DIC test were imported into ImageJ v1.46. The crack was identified by thresholding according to the gray value histogram, converted to a binary image and the crack opening displacement along the crack wake was calculated using Matlab 2012a.

2.4. Resistance-curve measurement

The pre-cracked HAH and RAR test-pieces were used to measure the R-curve for the hydrated and dry conditions. A digital camera attached to an optical microscope with a 10× objective lens was used to capture the crack extension. The test-pieces were loaded at the rate of 2 μm/s. According to the ASTM standard [53], the expression for the nominal mode-I stress intensity factor, K_1, for a compact tension test-piece is given by:

$$K_I = \frac{P}{B\sqrt{W}} \frac{(2+\alpha)}{(1-\alpha)^{3/2}} (0.886 + 4.64\alpha - 13.32\alpha^2 + 14.72\alpha^3 - 5.6\alpha^4) \quad (1)$$

where P is the applied load, B is the test-piece thickness, W is the test-piece width, α is the ratio which equals to a/W, a is the effective crack length. A drawback of the experimental set-up is that the hydrated test-piece could not be submerged in the distilled water because this hinders the optical measurement. Accordingly, some low level of near-surface drying out may have occurred during the tests (~7 min duration).

2.5. Statistical analysis

The variance in the strain measurement has been evaluated using a standard deviation analysis along the distance head of the crack tip. COD data is fitted with least-square regression (OriginPro 2015, OriginLab Corp) to extract the effective stress intensity factor, with an R-square factor above 0.9. The variance in the effective stress intensity factor is expressed in terms of the standard deviation at each load level.

3. Results

3.1. Crack-tip strain measurement

3.1.1. RAR Test-piece: crack growth parallel to the tubules

The total crack-tip strain field in the y-direction, ε_{yy}^{tot}, (i.e. perpendicular to the crack plane) was measured by DIC during the incremental loading and unloading for the RAR test-piece in the hydrated condition (Fig. 2a–d). The region behind the crack tip has been masked out to reduce the computational load. It is evident that upon unloading from $K^{appl} = 0.65\,MPa\sqrt{m}$ and $0.83\,MPa\sqrt{m}$ significant remnant strains ε_{yy}^{rem} remain. These strains include both inelastic strain ε_{yy}^{pl}, presumably resulting largely from crack-tip plasticity (micro-cracking, though not detected, could also contribute to inelastic strain), and an elastic strain ε_{yy}^{el} [54]. The elastic strain will give rise to a residual stress arising from the plastic misfit generated by the crack-tip stress field. Upon unloading, the matrix beyond the inelastically extended crack-tip zone exerts a compressive stress on the crack-tip zone, which is balanced by a distribution of tensile elastic strain outside the inelastic zone. Unsurprisingly, both ε_{yy}^{tot} (Fig. 2b) and ε_{yy}^{rem} (Fig. 2d) increased significantly as the load was increased.

By contrast, no significant crack tip plasticity, ε_{yy}^{pl}, was generated at $K^{appl} = 0.65\,MPa\sqrt{m}$ in the dry condition (Fig. 2e) as indicated by the very low level ε_{yy}^{rem} upon unloading (Fig. 2g). In fact much lower ε_{yy}^{rem} were evident upon unloading (Fig. 2h) even for loads much larger than for the hydrated case (Fig. 2f, $K^{appl} = 1.17\,MPa\sqrt{m}$).

3.1.2. HAH Test-piece: crack growth parallel to the plane of the collagen fibers

The crack-tip strain fields were also mapped for the HAH test-pieces tested under dry and hydrated conditions and the results are shown in Fig. 2i–n. In the hydrated condition a much lower ε_{yy}^{tot} is observed at $K^{appl} = 0.65\,MPa\sqrt{m}$ (Fig. 2i) than for the RAR case (Fig. 2a). At the higher load (Fig. 2j, $K^{appl} = 1.2\,MPa\sqrt{m}$), ε_{yy}^{tot} is more extensive, but is still characterized by a very small ε_{yy}^{rem} (Fig. 2l) suggestive of a predominantly elastic crack-tip stress field under load. As for the dry HAH test-piece, very little crack-tip plasticity is observed under dry conditions (Fig. 2m,n).

In order to undertake a quantitative analysis of the strain fields, the crack-tip strains, ε_{yy}^{tot}, along the crack plane ($y = 0$), have been plotted as a function of distance from the crack-tip for all the test-pieces (Fig. 3). This confirms that the hydrated test-pieces show much higher strains than the dry ones for similar stress intensities along with a much higher ratio of ε_{yy}^{rem} to ε_{yy}^{tot}, indicative of more extensive crack-tip plasticity. In the elastic (far-field) regime the hydrated sample strains more than the dry one implying a lower Young's modulus in accordance with previous observations [34–36]. The Young's modulii of the dry test-pieces were measured to be 13.6 (±1.9,

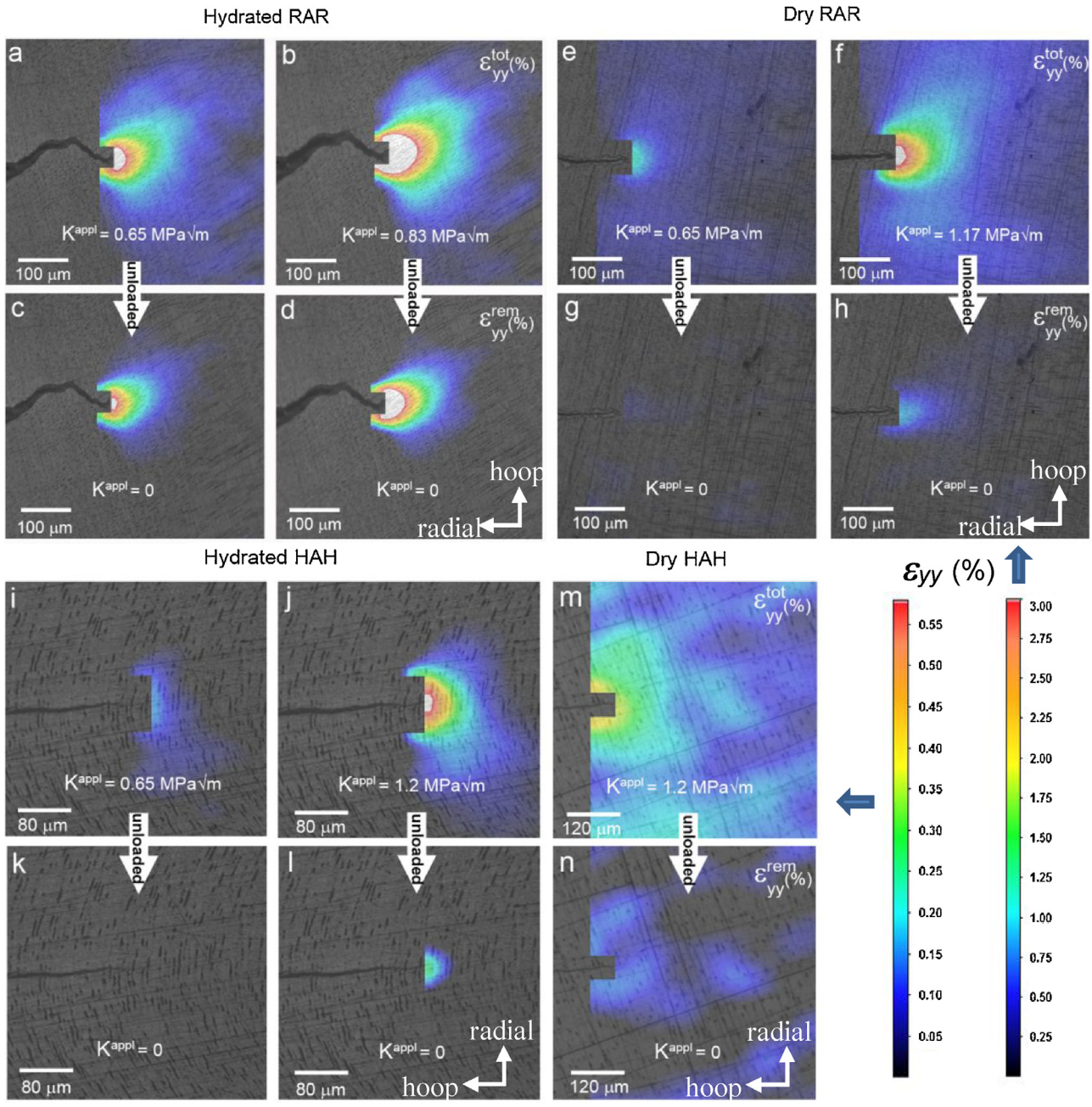

Fig. 2 – Total crack-tip strain measured by DIC for (a–d) RAR test-piece in the hydrated condition and (e–h) dry condition, with loaded (top) and unloaded (bottom); HAH test-piece in (i–l) hydrated and (m–n) dry condition, both loaded (top) and unloaded (bottom); the (colour) strain maps are superimposed on the (black and white) optical microscopic images collected for the DIC measurement.

n > 20) and 15.6 (±2.3, n > 20) GPa in the RAR and HAH orientations from our previous nanoindentation test [55]. A simple comparison of the strains would suggest that the Young's moduli for the hydrated test-pieces are around 6.0 (±0.7) and 13.8 (±2.1) GPa in RAR and HAH orientations respectively. These results agree well with the Young's modulus reported previously for dry elephant dentin (12–17 GPa [2,19]). Break and Currey [56] also confirmed that hydration can reduce the Young's modulus by 30–60% compared to that for dry samples.

3.2. *Crack opening displacement (COD) measurement*

The effective stress intensity factor K^{eff} experienced at the crack-tip can be inferred from the ΔCOD data (i.e. relative to the crack opening displacement at zero applied load) [54]:

$$\Delta u(r) = 8\frac{K^{eff}}{E'}\sqrt{\frac{r}{2\pi}} \quad (2)$$

where E' is equal to E under plane stress conditions and $E/(1-\nu^2)$ under plane strain conditions and $\Delta u(r)$ is the ΔCOD

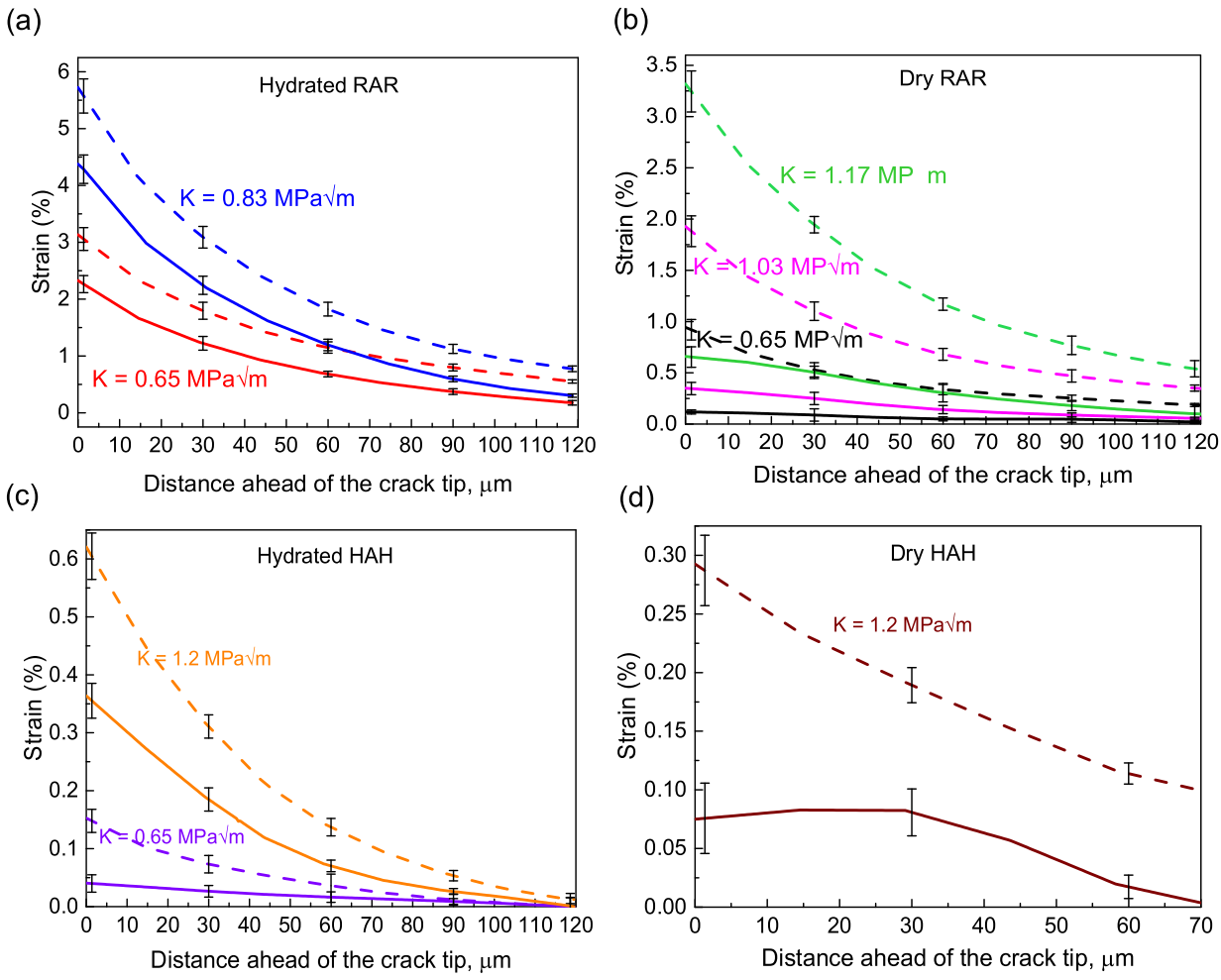

Fig. 3 – The strain at the crack-plane, ε_{yy}^{tot} (y = 0) plotted as a function of distance ahead of the crack tip in the loaded (dashed) and unloaded (solid) conditions for (a) RAR hydrated test-piece (b) RAR dry test-piece (c) HAH hydrated test-piece (d) HAH dry test-piece. Note the very different strain scales.

Table 1 – Comparison of the inferred K^{eff} and the applied K^{appl} (MPa$\sqrt{m}$).

	Hydrated RAR (n = 3)		Dry RAR (n = 3)		Hydrated HAH (n = 3)		Dry HAH (n = 3)
K^{appl}	0.65	0.83	0.65	1.17	0.65	1.2	1.2
K^{eff}	0.31 (±0.05)	0.52 (±0.09)	0.37 (±0.06)	0.95 (±0.13)	0.57 (±0.08)	1.02 (±0.11)	1.10 (±0.14)
K^{eff}/K^{appl}	48% (±7%)	62% (±10%)	58% (±9%)	78% (±11%)	88% (±12%)	90% (±9%)	91% (±12%)

at a distance *r* behind the crack tip. The COD data in Fig. 4a and b broadly correspond to a $\sqrt{r}$ relationship in all cases with the hydrated samples exhibiting significantly larger crack openings than the dry ones, and the RAR test-pieces show larger COD than the HAH samples. It also noteworthy that the residual openings for the hydrated test-pieces are much larger than those for the dry test-pieces. These results correlate with the residual crack-tip strain field ε_{yy}^{rem} results and indicate that plasticity near the crack-tip results in crack-tip blunting and increased residual opening especially for the hydrated samples. These measured displacements are very small leading to some measurement scatter. However, close inspection of the curves show that much of the point to point scatter in Fig. 4a and b is carried over from the unloaded to the loaded curves suggesting that this is not random measurement scatter but related to the meandering crack surfaces and local bridging effects. The changes in COD between the loaded and the unloaded cases are shown in Fig. 4c and d which inevitably are sensitive to measurement scatter. Nevertheless given the expected $\sqrt{r}$ it is possible to infer the effective stress intensity factors K^{eff} by fitting the responses to Eq. (2). These are compared with those nominally applied (K^{appl}) in Table 1 from which it is clear that the shielding effect for RAR test-pieces are significant with the hydrated ones around 10% greater than for the dry ones. It is also evident that the bridging stresses for the hydrated and dry RAR test-pieces remain almost constant at different loads. By contrast, for the HAH orientation, the hydrated and dry test-pieces show little evidence of crack-tip shielding nor little benefit arising from hydration.

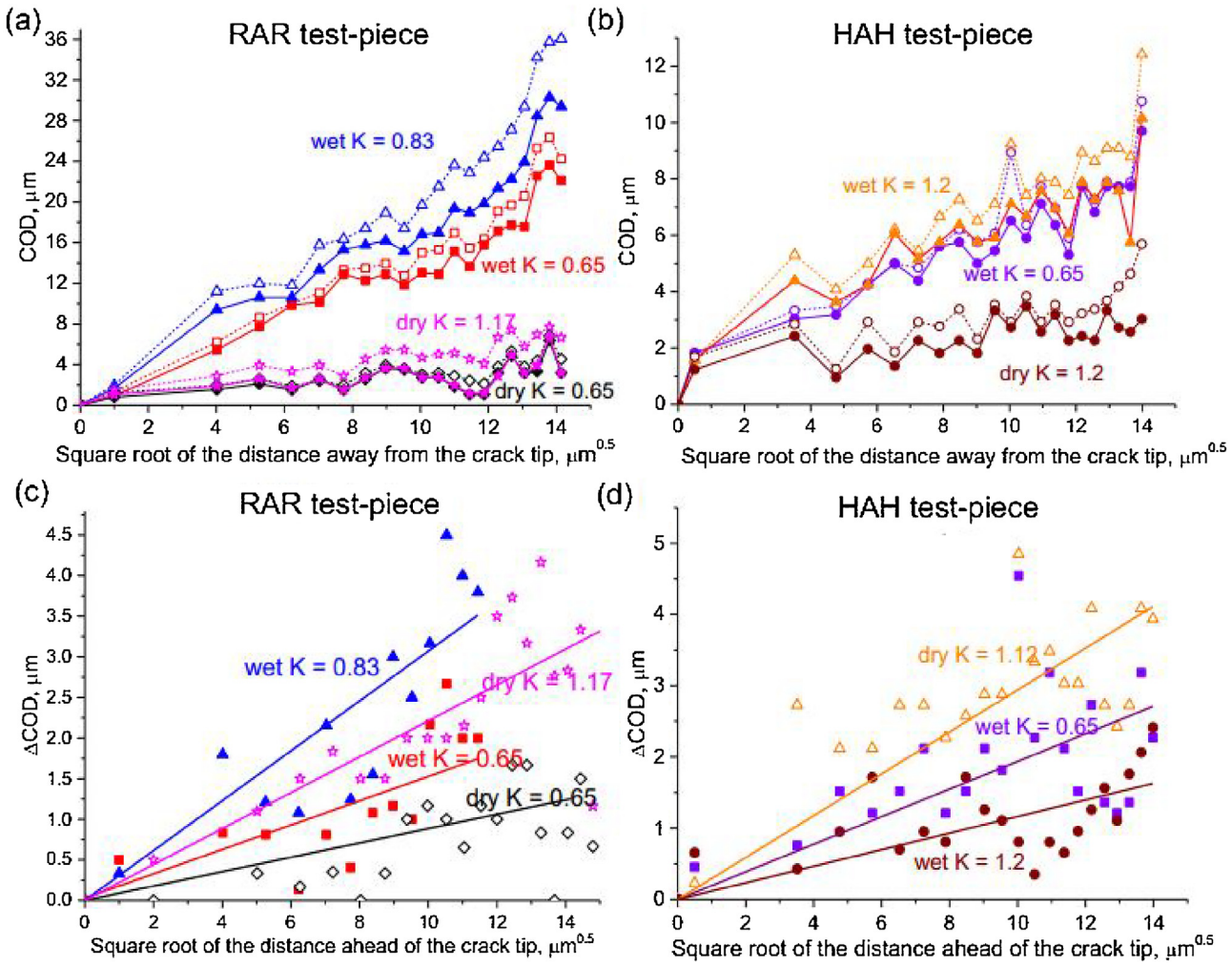

Fig. 4 – The crack opening displacement (COD) under load (dashed line, open symbol) and after unloading (solid line, bold symbol) for (a) the RAR oriented test-pieces and (b) the HAH oriented test-pieces. After subtraction of the unloaded curves from the loaded ones, the elastic ΔCODs were obtained for (c) RAR test-pieces and (d) HAH test-pieces. Bold and open symbols in (c) and (d) represent hydrated (i.e. wet) and dry test-pieces respectively. The data points were fitted by least square regression method to estimate K^{eff} for all the load cases using Eq. (2).

3.3. *Plastic zone size and model predictions*

In order to characterise the intrinsic toughening it is useful to be able to quantify the plastic zone ahead of the crack. It is challenging to measure the plastic zone size for brittle materials because of the difficulty identifying a conventional yield strain ε_y. We believe this study to be the first to experimentally estimate the yield strain/stress and plastic zone size at the crack-tip for dentin materials. Our approach is based on Irwin's model [57], which estimates the plastic zone according to the strain balance inside and outside of the plastic zone, assuming that the strain distribution outside the plastic zone along the crack line follows the elastic *K*-field $\sigma = \frac{K_I}{\sqrt{2\pi x}}$, while the elastic strain in the plastic zone equals the yield strain. The occurrence of the inelastic deformation at the crack-tip on loading is often associated with a local residual compression upon unloading, resulting in a residual elastic stress field: namely a compressive elastic stress field within the inelastic zone, which is balanced by a tensile elastic stress outside the inelastic zone. Thus a residual elastic strain curve (dotted line) can be inferred for each total strain curve (dashed line) by subtracting the elastic strain (*K*-field) from the total strain curves. If we assume ideal plasticity and elastic unloading we can identify a yield strain, ε_y, such that the observed total strains at K_{max} (dashed line) and $K = 0$ (solid line) in Fig. 5 are consistent with a balance of the residual elastic strain (stress) at $K = 0$ (dotted line) [58]. Here the yield strain was estimated at each load independently. The best-fit ε_y are plotted for the two test-pieces at each load in Fig. 5 where it is evident that, as one might expect, the yield strain obtained for a given sample does not vary with increasing load (though the plastic zone naturally does) giving confidence in the analysis method. Further the yield strain is broadly similar for the hydrated and dry cases (0.90% vs. 0.83% respectively). Taking the measured (elastic) strains at the boundary of plastic/elastic zone for the hydrated ($\varepsilon_{xx} = 0.12\%$, $\varepsilon_{yy} = 0.90\%$) and dry ($\varepsilon_{xx} = 0.05\%$, $\varepsilon_{yy} = 0.83\%$) RAR test-pieces, the tri-axial yield strengths are estimated to be 43 MPa and 78 MPa for the hydrated and dry

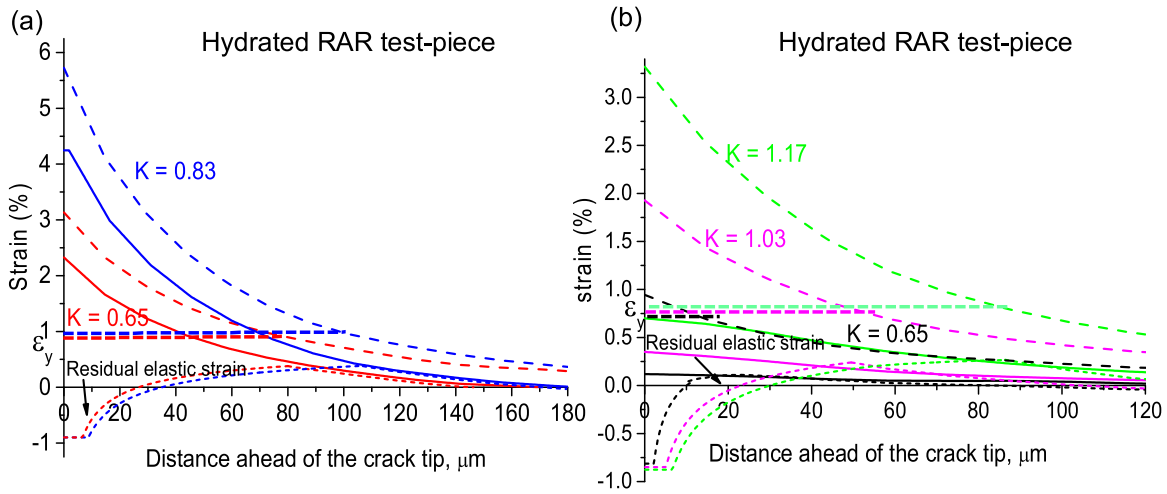

Fig. 5 – The measured residual strain and the estimated residual elastic strain at unloaded condition for (a) hydrated and (b) dry RAR test-piece. The estimated elastic strain curves were obtained by defining a yield strain ε_y which gives stress balance in the unloaded condition. (Dashed curve: loaded strain; solid curve: unloaded strain; dotted curve: residual elastic strain; straight dashed line: yield stress level).

test-pieces, using Hooke's law under the plane strain assumption and the von Mises yield criterion. The yield strength of the hydrated RAR test-piece in elephant dentin is slightly lower than previously reported values (50–65 MPa [19]). Few researchers have recorded the yield strength of dry elephant dentin, but the reported ultimate strength (98 ± 18 MPa) [59] could be considered as an upper bound.

It is useful to compare the plastic zones of hydrated RAR test-piece determined experimentally with the ones predicted empirically based on Irwin's model (Eq. (3)) and Dugdale's model [60]. In contrast to the strain balance theory described in Irwin's model (which is aligned with our approach), Dugdale's model treats the plastic zone as an extension of a physical crack with the closure yield stress acting on the extended crack faces; thereby stresses are finite at the effective crack-tip. The plastic zone is calculated by negating the applied crack-tip stress intensity with the integration of yield stress along the yield zone and expressed as (Eq. (4))

$$r_Y = \frac{1}{\pi}\left(\frac{K_I}{\sigma_Y}\right)^2 \tag{3}$$

$$r_Y = \frac{\pi}{8}\left(\frac{K_I}{\sigma_Y}\right)^2 \tag{4}$$

Table 2 presents the plastic zones of hydrated RAR inferred from Fig. 5 as well as the predictions using the measured yield strains from the Irwin and Dugdale models. It is evident that the plastic zone sizes are significantly larger for the hydrated samples relative to the dry ones. The experimentally measured yield zone displays better agreement with Irwin's model than Dugdale's.

3.4. *R-curve responses*

In order to quantify the crack shielding as the crack extends, R-curves were measured for the two test-piece orientations in

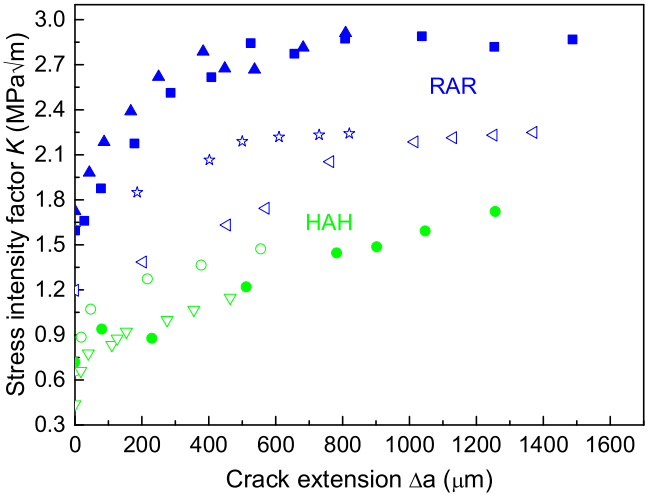

Fig. 6 – Crack resistance (R) curves for the RAR (blue) and HAH (green) orientation test-pieces in hydrated (bold symbol) and dry (open symbol) conditions. The crack length for RAR test-pieces are corrected by the plastic zone sizes measured and extrapolated at incremental loads.

the hydrated and dry conditions. R-curves of the hydrated and dry RAR test-pieces were plotted after crack length correction based on the plastic zone size measured above. The plastic zone size at incremental loads were extrapolated according to the relationship $r_Y \sim K^2$. Unsurprisingly, the results summarized in Fig. 6 show clear differences according to the test-piece orientation (RAR and HAH). RAR test-pieces tended to have a much higher initiation fracture toughness ($K_0 \approx 1.2$ MPa$\sqrt{}$m) compared to the HAH test-pieces ($K_0 \approx 0.8$ MPa$\sqrt{}$m). Although both sample types exhibit rising R-curve behavior, the RAR curves show more extensive sub-critical growth and a higher K_{IC} (2.1–2.9 MPa$\sqrt{}$m) compared to the HAH test-pieces (1.2–1.5 MPa$\sqrt{}$m). This is in a good agreement with the

Table 2 – The comparison of the experimentally measured yield strain, yield stress (in MPa), plastic zone (in μm) and the predictions using ε_y based on Irwin's and Dugdale's models for RAR test-piece.

	Hydrated (MPa$\sqrt{m}$) (n = 3)		Dry (MPa$\sqrt{m}$) (n = 3)		
	K = 0.65	K = 0.83	K = 0.65	K = 1.03	K = 1.17
Yield strain	0.9%			0.83%	
Yield stress	43			78	
Measured	78 (±5)	107 (±8)	15 (±3)	51 (±6)	84 (±6)
Irwin	72	118	22	59	67
Dugdale	88	145	27	72	82

reported results from Nalla et al. [19] and Kruzic et al. [32]. In the HAH case the R-curve rises gradually but it would appear that the shielding zone is not as effective. It is also meaningful to compare the R-curve response for the hydrated and the dry test-pieces: for the hydrated RAR test-pieces, the rising regime is steeper than the dry ones, and the plateaus are approximately 40% higher. However, for the HAH test-pieces the hydrated test-piece demonstrates higher fracture toughness and longer sub-critical growth distance. The mechanisms of the R-curve response will be discussed in Section 4.3.

4. Discussion

4.1. *Effect of crack orientation on extrinsic shielding*

The crack opening displacement (COD) response shows that for the RAR test-pieces the effective stress intensity factors are significantly lower than nominally applied, but not for the HAH test-pieces. This suggests much greater extrinsic shielding (bridging) in the former case, which reduces the stress driving force available for crack extension. Conventional cross sections (Fig. 7a–c) of the crack for the RAR test-piece do show some evidence of crack bridging which appears to be guided somewhat by the tubules. However the picture becomes much clearer when the crack is viewed in 3D from the tomograph (Fig. 7d) or through virtual hoop–axial cross-sections (Fig. 7e–g). These show clearly that the crack actually propagates not as a single crack, but as a series of overlapping 'fingers', as observed previously by Burnett et al. [61] by CT for stress corrosion in Al alloys. These branched cracks (delineated by different colours in Fig. 7d) initiate at different locations from the crack front and form a continuous chain of laterally bridging ligaments across the thickness of the test-piece. It is likely that these fingers are the result of (radial-axial) microcracks that emanate from the tubules in the axial direction (as in Fig. 1c). While these bridges are sometimes captured in conventional hoop-axial cross sections, their efficacy and number would be underestimated. Fig. 7e–g shows that the formed ligaments ultimately rupture with increasing distance from the crack tip due to the increased crack opening and merge to form a single dominant crack. It can be seen from Fig. 7d that the finger-like bridging zone extends ca. 400 μm from the crack tip before the ligaments rupture. The fracture surface in Fig. 7h clearly shows the uneven (layered) fracture plane due to the bridging, which is instigated by the microcracks at the tubules aligned in the radial direction. Moreover, the magnified image clearly shows the collagen fibrils bridging the microcracks (Fig. 7i), indicating that this also contributes to crack shielding.

The role of the micro-cracking local to the tubules (evident in Fig. 7h) in bringing about ligament bridging for the RAR specimen is contrasted with the crack morphology for the HAH sample (Fig. 8a). Here the axial–radial microcracks initiated by the tubules are much less effective. This is because the tubules run vertically and so cannot 'guide' the crack in a tortuous way or create parallel cracks and bridges, as in the RAR orientation. Furthermore, as seen in Fig. 8b, little collagen pull-out is observed because the collagen fibrils lie in planes on the fracture surface (Fig. 8c and d).

4.2. *Intrinsic shielding and the effect of moisture*

It is known that collagen fibrils not only can help to bridge the crack-tip, but also have a significant role in increasing the deformability and fracture toughness [62–64]. This is known as intrinsic shielding, which describes the inherent capability of the dentin to 'plastically' deform/absorb energy as the crack proceeds. In both the hydrated and dry conditions the crack-tip strains (ε_{yy}^{tot}) in the RAR orientation are as much as 10× higher than those for the HAH test-pieces, accompanied by larger crack-tip opening as well (Fig. 4a and b). Moreover, the RAR test-piece also shows a blunt crack tip (see Fig. 2b), providing further evidence of a higher strain to failure in the RAR orientation. This distinct difference of crack-tip strain and opening could be related to the orientation of the fibrils ahead of the crack-tip. The 'plasticity' is accentuated by a moist environment with the hydrated test-pieces exhibited crack-tip strains twice as large as the dry test-piece for both types of test-pieces. This is likely to be because of the well catalogued effect of moisture on the collagen which plasticizes the tissue, although the mechanism is the subject of debate [65–67] and is beyond the scope of this study.

4.3. *R-curve and the extrinsic shielding*

The R-curve for the RAR test-pieces showed a more pronounced rise in the fracture toughness K_{IC} with crack extension (Δa) than the HAH test-pieces. Both hydrated and dry RAR test-pieces show the rising of the R-curve followed by a plateau. The higher initiation fracture toughness K_0 for hydrated RAR indicates a larger strain to failure and more effective intrinsic shielding. This may be attributed to the effect of moisture in plasticising the collagen fibrils so that the deformability of the dentin is enhanced, as is supported by the crack-tip strain measurement in this study. The rise of the fracture toughness derives from the fact that the shielding

from ligament bridging initially builds up as the crack grows and thus requires significant crack propagation to reach maturity. The R-curve then becomes flat when there is a balance between the formation of new bridges and the breaking of existing ones. The initial rapid rise in the R-curve in Fig. 6 for the dry RAR samples is consistent with the observations of crack bridging indicating that the ligament bridging 'fingers' extend around 3–400 μm behind the crack. The faster rise and higher critical fracture toughness K_{IC} of the hydrated RAR test-pieces may be explained by the plasticised collagen fibrils so that the ligaments fail at larger crack openings. Consistent with Fig. 8, the HAH samples on the other hand show both a low initiation toughness and no steep rise in the R-curve suggesting that the bridging length is very short. It needs to be pointed out that the magnitude of the bridging stress is dependent on the experiment method. For instance, the values measured in this study using COD method are consistent with the ones measured by load appliance calculation, but much lower than the ones predicted using a theoretical model [32], in which the area fraction of the ligament bridging is difficult to validate.

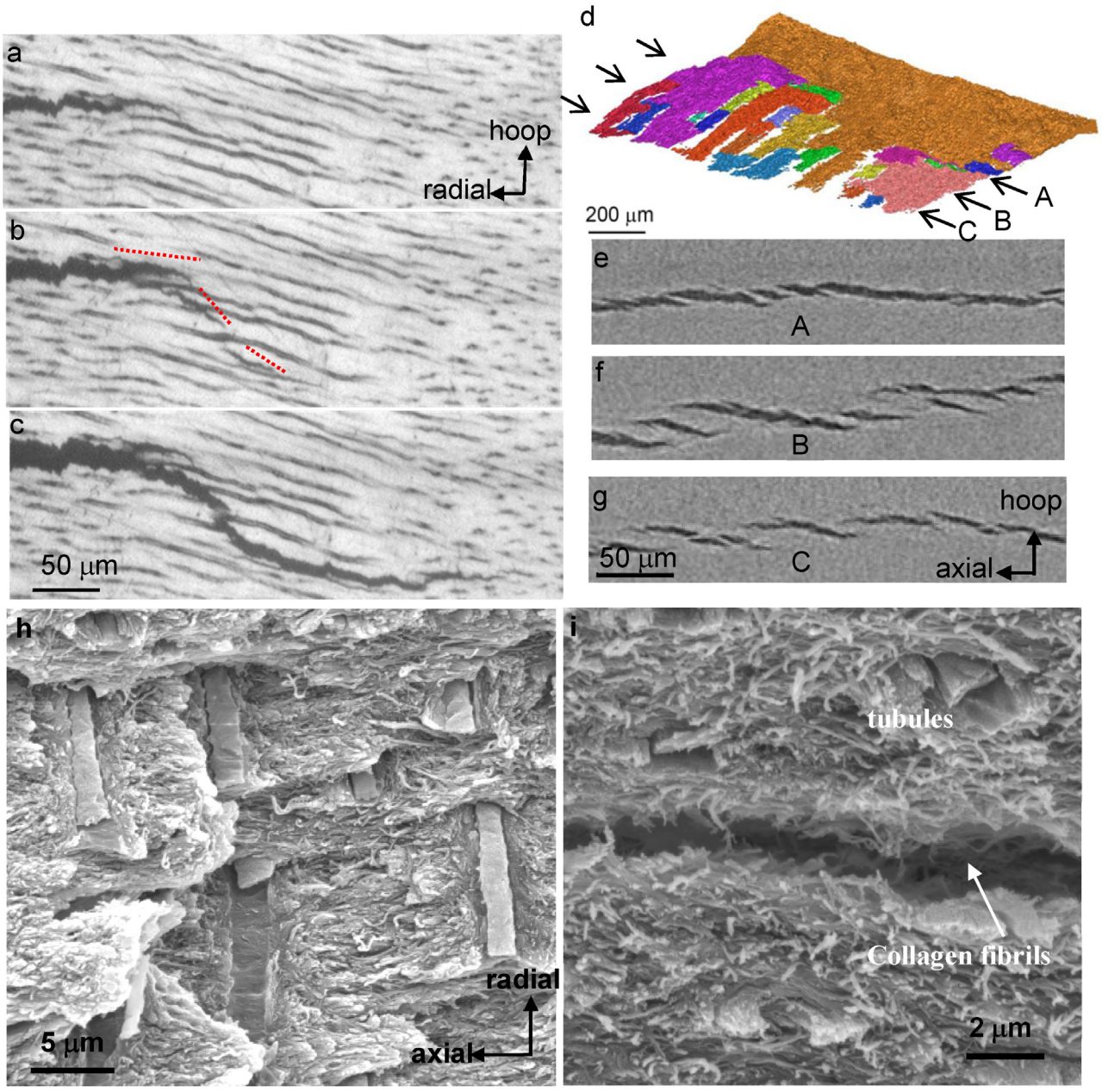

Fig. 7 – The extrinsic shielding mechanisms in RAR. (a–c) Optical images of side surface showing the formation of the uncracked-ligament bridging during crack propagation; (d) crack morphology of the dry RAR test-piece in 3D reconstructed from an X-ray computed tomography scan. Branched cracks are labelled with different colours; (e–g) X-ray computed tomographic slice showing the ligament bridging lateral to the crack front across the thickness of the test-piece at (e) 300 μm (f) 200 μm (g) 100 μm behind the crack front; (h) SEM image showing the fracture surface and its intersection with many tubules; (i) magnified fracture surface showing the evidence of collagen fibrils bridging inside a small crack.

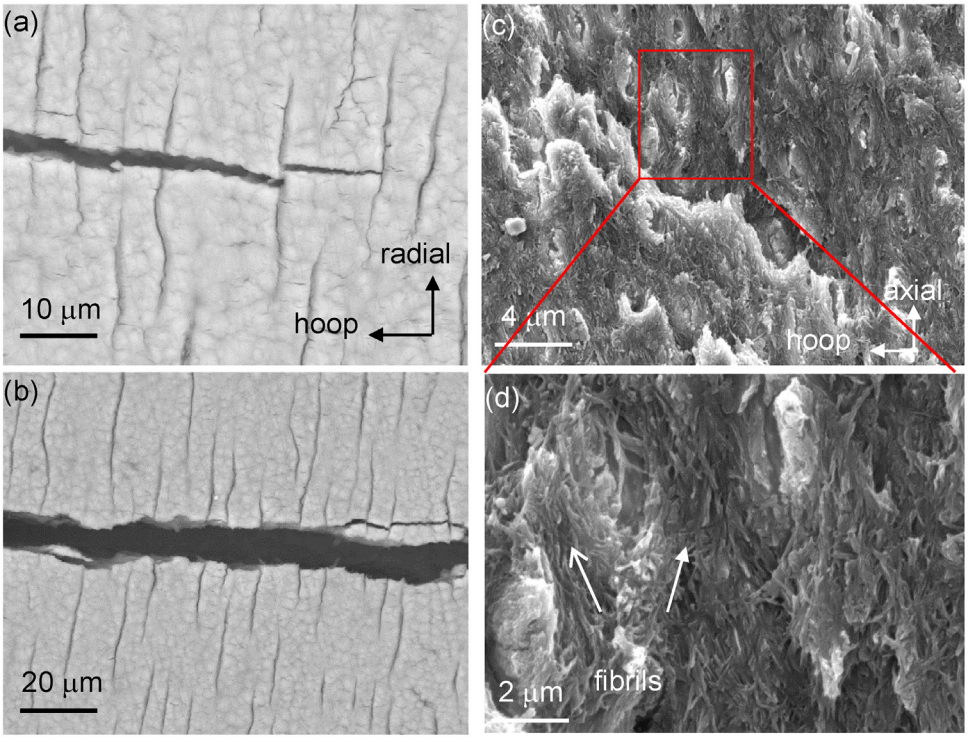

Fig. 8 – The SEM images showing the crack morphology of HAH test-piece. (a) While there is some crack deflection caused by radial–axial cracking at the tubules, the crack is largely a single dominant crack; (b) furthermore the fact the collagen fibrils lie in the hoop–axial plane (see Fig. 1f) mean that there is relatively little pull-out of the collagen fibrils; (c) SEM image showing the fracture surface; (d) +/−10° in-plane collagen fibrils are observed on the fracture surface surrounding the tubule cross sections.

As we have seen above, the formation of axial–radial micro-cracks in elephant dentin aligned with the semi major axis of the tubules is almost certainly associated with the orientation of the collagen fibrils (varying by +/−10° in-plane parallel to the tubule semi-major axis). This makes tusk highly anisotropic perpendicular to the tubule axis. As a consequence, the crack propagation resistance is significantly lower along the axial direction of the tusk than perpendicular to it. This is reasonable from an evolutionary design point of view, as the tusk is prone to experience flexural stress by nature which might otherwise lead to the tusk fracturing perpendicular to its axis. By contrast, this is not the case for human dentin where the collagen fibrils are arranged in a random mat perpendicular to the tubules. Moreover, the peritubular dentin could inhibit cracking from the tubules. Accordingly, human dentin is often viewed as transversely isotropic relative to the tubule axis.

5. Conclusions

This paper examines the intrinsic toughening in terms of the elastic-plastic strain field ahead of the crack tip by DIC and the extrinsic toughening behind the advancing crack in terms of 3D CT images of crack bridging and its effect on the R-curve behaviour. It is noteworthy that conventional 2D cross sections of the crack do not adequately reveal the fragmentation of the advancing crack into 'fingers' parallel to the crack propagation direction. Not only does 3D X-ray CT reveal these the presence of these overlapping fingers which provide very effective crack bridging, virtual cross-sections perpendicular to the propagation direction provide a simple way of confirming how far behind the crack, and at what degree of crack opening, the ligaments rupture to form a single primary crack.

This paper presents the first maps of the strain fields in elephant dentin local to the crack-tip and an attempt to measure the 'plastic' zone size. The effect of hydration on the intrinsic and extrinsic toughening mechanisms has been assessed in terms of crack-tip plasticity, strain field and R-curve. Our results clarify the significance of hydration on the plasticity near the crack-tip and highlight the critical role of the organic collagen and tubule induced micro-cracking in crack-tip shielding. Several important conclusions are drawn as follows:

With respect to the intrinsic toughening ahead of the crack, the role of the collagen is of primary importance:

1. For cracks grown normal to the length of the tusk (RAR), the maximum strain at the crack-tip was 10 times larger than for cracks growing in the hoop–axial plane, in the hoop direction (HAH), under both hydrated and dry conditions. The crack-tip strain to failure for the hydrated test-pieces was twice as large as the dry ones. Key factors contributing to these differences are the hydration and orientation of the collagen relative to the crack plane.
2. The plastic zones were determined directly from the strain fields. We identified plastic zones of 78 μm at $K^{appl} = 0.65\ \text{MPa}\sqrt{\text{m}}$ and 107 μm at $K^{appl} = 0.83\ \text{MPa}\sqrt{\text{m}}$ in the

hydrated and 10 μm at $K^{appl} = 0.65\,MPa\sqrt{m}$ and 84 μm at $K = 1.17\,MPa\sqrt{m}$ for the dry RAR test-pieces. In contrast the plastic strains for HAH test-pieces were negligible in wet and dry conditions. Tri-axial yield strengths were measured to be 43 MPa and 78 MPa for hydrated and dry RAR test-pieces respectively. Ahead of the plastic zone, the elastic strains matched well with theoretical expectations.

3. Hydration of the collagen significantly improves the intrinsic toughness in terms of larger crack-tip elastic/plastic strain, crack-tip blunting and higher $\Delta K_{IC}/\Delta a$ rate, compared with the dry test-pieces.

With respect to the extrinsic toughening behind the crack, crack bridging is of primary importance and collagen pull-out is, of itself, less important:

1. Extrinsic crack tip shielding meant that the crack-tip stress intensity factors at the crack tip were only 48% and 60% of the nominally applied stress intensity for the hydrated and dry RAR test-pieces.
2. For the cracks grown in the RAR orientation, the formation of axial–radial micro-cracks that emanate axially from the tubules causes significant ligament bridging once a mature crack has developed. These cause the crack to break up into 'fingers' that are maintained up to around 400 μm behind the crack front before they rupture. This is reflected in a rising R-curve response until the crack has developed to 3–400 μm in length. While at the micron scale collagen fibril pull-out is also observed, this is thought to be of secondary importance to the mesoscale bridges. The hydrated RAR samples have a critical fracture toughness K_c that is 40% larger than in the dry case, which may be affected by collagen plasticity which means that in the hydrated case the bridges are more plasticised and fail later at larger crack openings.
3. The HAH test-pieces show almost no ligament bridging and a negligible difference between hydrated and dry ones. This explains why there was almost no significant crack-tip shielding and the R-curve response shows no sudden rise with increasing length.

Acknowledgements

We acknowledge the Engineering and Physical Science Research Council (EPSRC) for funding the Henry Moseley X-ray Imaging Facility through grants (EP/F007906/1, EP/F001452/1, EP/I02249X, EP/M010619/1, EP/F028431/1, and EP/M022498/1) within the Royce Institute. PJW acknowledges support from the European Research Council grant No. 695638 CORREL-CT. XL is grateful to China Scholarship Council and the University of Manchester for funding his PhD. XL appreciates the help from Mr. Brian Daber and Prof. David Watts for their contribution to sample preparation.

REFERENCES

[1] Ritchie RO. Mechanisms of fatigue-crack propagation in ductile and brittle solids. Int J Fract 1999;100:55–83.
[2] Kruzic J, Nalla RK, Kinney JH, Ritchie RO. Crack blunting, crack bridging and resistance-curve fracture mechanics in dentin: effect of hydration. Biomaterials 2003;24:5209–21.
[3] Locke M. Structure of ivory. J Morphol 2008;269:423–50.
[4] Nalla RK, Imbeni V, Kinney JH, Staninec M, Marshall SJ, Ritchie RO. In vitro fatigue behavior of human dentin with implications for life prediction. J Biomed Mater Res A 2003;66A:10–20.
[5] Moyes AB, Doidge DW. Composition of the mineral phase of dentin in southern elephant seal and Antarctic fur-seal teeth. Br Antarctic Surv Bull 1984;8:1–4.
[6] Mills A. Structural and chemical organization of teeth. Elsevier; 2014.
[7] Miles AEW, Boyde A. Observations on structure of elephant ivory. J Anat 1961;95:450.
[8] Raubenheimer EJ, Dauth J, Dreyer MJ, Smith PD, Turner ML. Structure composition of ivory of the African elephant (Loxodonta-Africana). S Afr J Sci 1990;86:192–3.
[9] Marshall GW, Inai N, Magidi ICW, Ballouch M, Kinney JH, Tagami J, et al. Dentin demineralisation: effects of dentin depth, pH and different acids (vol 13, pg 338, 1997). Dent Mater 1998;14:383.
[10] Albéric M, Dean MN, Gourrier A, Wagermaier W, Dunlop JWC, Staude A, et al. Relation between the macroscopic pattern of elephant ivory and its three-dimensional micro-tubular network. PLoS One 2017;12:e0166671.
[11] Povar ML. The structural and chemical organization of teeth. J Am Vet Med Assoc 1967;151:1211.
[12] Su XW, Cui FZ. Hierarchical structure of ivory: from nanometer to centimeter. Mater Sci Eng C-Bio S 1999;7:19–29.
[13] Alberic M. Etude chimique et structurale de l'ivoire d'éléphant moderne etancien; PhD Thesis, 2014.
[14] Lu X. Characterisation of the anisotropic fracture toughness and crack-tip shielding mechanisms in elephant dentin. University of Manchester; 2015. PhD thesis.
[15] Arola D, Rouland JA, Zhang D. Fatigue and fracture of bovine dentin. Exp Mech 2002;42:380–8.
[16] Ivancik J, Neerchal NK, Romberg E, Arola D. The reduction in fatigue crack growth resistance of dentin with depth. J Dent Res 2011;90:1031–6.
[17] Iwamoto N, Ruse ND. Fracture toughness of human dentin. J Biomed Mater Res A 2003;66A:507–12.
[18] Bonfield W, Li CH. Deformation and fracture of ivory. J Appl Phys 1965;36:3181.
[19] Nalla RK, Kinney JH, Ritchie RO. Effect of orientation on the in vitro fracture toughness of dentin: the role of toughening mechanisms. Biomaterials 2003;24:3955–68.
[20] Watanabe LG, Marshall GW, Marshall SJ. Dentin shear strength: effects of tubule orientation and intratooth location. Den Mater 1996;12:109–15.
[21] Arola DD, Reprogel RK. Tubule orientation and the fatigue strength of human dentin. Biomaterials 2006;27:2131–40.
[22] Ivancik J, Arola DD. The importance of microstructural variations on the fracture toughness of human dentin. Biomaterials 2013;34:864–74.
[23] Bajaj D, Sundaram N, Nazari A, Arola D. Age, dehydration and fatigue crack growth in dentin. Biomaterials 2006;27:2507–17.
[24] Arola D, Reprogel RK. Effects of aging on the mechanical behavior of human dentin. Biomaterials 2005;26:4051–61.
[25] Koester KJ, Ager III JW, Ritchie RO. The effect of aging on crack-growth resistance and toughening mechanisms in human dentin. Biomaterials 2008;29:1318–28.
[26] Foulk III JW, Cannon RM, Johnson GC, Klein PA, Ritchie RO. A micromechanical basis for partitioning the evolution of grain bridging in brittle materials. J Mech Phys Solids 2007;55:719–43.

[27] Koester KJ, Barth HD, Ritchie RO. Effect of aging on the transverse toughness of human cortical bone: evaluation by R-curves. J Mech Behav Biomed Mater 2011;4:1504–13.
[28] Kruzic JJ, Satet RL, Hoffmann MJ, Cannon RM, Ritchie RO. The utility of R-curves for understanding fracture toughness-strength relations in bridging ceramics. J Am Ceram Soc 2008;91:1986–94.
[29] Launey ME, Ritchie RO. On the fracture toughness of advanced materials. Adv Mater 2009;21:2103–10.
[30] Ritchie RO, Nalla RK, Kruzic JJ, Ager III JW, Balooch G, Kinney JH. Fracture and ageing in bone: toughness and structural characterization. Strain 2006;42:225–32.
[31] Zimmermann EA, Launey ME, Ritchie RO. The significance of crack-resistance curves to the mixed-mode fracture toughness of human cortical bone. Biomaterials 2010;31:5297–305.
[32] Kruzic JJ, Nalla RK, Kinney JH, Ritchie RO. Crack blunting, crack bridging and resistance-curve fracture mechanics in dentin: effect of hydration. Biomaterials 2003;24:5209–21.
[33] Kahler B, Swain MV, Moule A. Fracture-toughening mechanisms responsible for differences in work to fracture of hydrated and dehydrated dentine. J Biomech 2003;36:229–37.
[34] Guidoni G, Denkmayr J, Schöberl T, Jäger I. Nanoindentation in teeth: influence of experimental conditions on local mechanical properties. Philos Mag 2006;86:5705–14.
[35] Bertassoni LE, Habelitz S, Kinney JH, Marshall SJ, Marshall Jr GW. Biomechanical perspective on the remineralization of dentin. Caries Res 2009;43:70–7.
[36] Huang T-JG, Schilder H, Nathanson D. Effects of moisture content and endodontic treatment on some mechanical properties of human dentin. J Endod 1992;18:209–15.
[37] Bertassoni LE, Swain MV. Influence of hydration on nanoindentation induced energy expenditure of dentin. J Biomech 2012;45:1679–83.
[38] Tiossi R, Lin L, Rodrigues RCS, Heo YC, Conrad HJ, de Mattos MdGC, et al. Digital image correlation analysis of the load transfer by implant-supported restorations. J Biomech 2011;44:1008–13.
[39] Chen TY-F, Huang P-S, Chuang S-F. Modeling dental composite shrinkage by digital image correlation and finite element methods. Opt Lasers Eng 2014;61:23–30.
[40] Thompson MS, Schell H, Lienau J, Duda GN. Digital image correlation: a technique for determining local mechanical conditions within early bone callus. Med Eng Phys 2007;29:820–3.
[41] Vaananen SP, Amin Yavari S, Weinans H, Zadpoor AA, Jurvelin JS, Isaksson H. Repeatability of digital image correlation for measurement of surface strains in composite long bones. J Biomech 2013;46:1928–32.
[42] ASTM Standard E1820-08a. Standard Test Method for Measurement of Fracture Toughness. West Conshohocken, PA, USA: ASTM International; 2008.
[43] Weiner S, Wagner HD. The material bone: structure-mechanical function relations. Annu Rev Mater Sci 1998;28:271–98.
[44] Halpin JC. Primer on Composite Materials Analysis, (Revised). CRC Press; 1992.
[45] Lieberman DE. Life history variables preserved in dental cementum microstructure. Science 1993;261:1162.
[46] Mobarak EH, El-Badrawy W, Pashley DH, Jamjoom H. Effect of pretest storage conditions of extracted teeth on their dentin bond strengths. J Prosthet Dent 2010;104:92–7.
[47] Kitasako Y, Burrow M, Nikaido T, Tagami J. The influence of storage solution on dentin bond durability of resin cement. Dent Mater 2000;16:1–6.
[48] Titley K, Chernecky R, Rossouw P, Kulkarni G. The effect of various storage methods and media on shear-bond strengths of dental composite resin to bovine dentine. Arch Oral Biol 1998;43:305–11.
[49] Secilmis A, Dilber E, Gokmen F, Ozturk N, Telatar T. Effects of storage solutions on mineral contents of dentin. J Dent Sci 2011;6:189–94.
[50] Addy M, Mostafa P. Dentine hypersensitivity. I. Effects produced by the uptake in vitro of metal ions, fluoride and formaldehyde onto dentine. J Oral Rehabil 1988;15:575–85.
[51] Quinta da Fonseca J, Mummery PM, Withers PJ. Full-field strain mapping by optical correlation of micrographs acquired during deformation. J Microsc 2005;218:9–21.
[52] Sutton MA, Orteu JJ, Schreier H. Image correlation for shape, motion and deformation measurements: basic concepts, theory and applications. Springer Science & Business Media; 2009.
[53] ASTM Standard E1820-01. Standard test method for measurement of fracture toughness. West Conshohocken, PA, USA: ASTM International; 2002.
[54] Withers PJ. Residual stress and its role in failure. Rep Prog Phys 2007;70:2211–64.
[55] Lu X. Unpublished results. University of Manchester; 2017.
[56] Break K, Currey J, Pond C, Ramsay M. The mechanical properties of the dentine and cement of the tusk of the narwhal Monodon monoceros compared with those of other mineralized tissues. Arch Oral Biol 1990;35:615–21.
[57] Irwin G. Plastic zone near a crack and fracture toughness; 1997.
[58] Lopez-Crespo P, Steuwer A, Buslaps T, Tai YH, Lopez-Moreno A, Yates JR, et al. Measuring overload effects during fatigue crack growth in bainitic steel by synchrotron X-ray diffraction. Int J Fatigue 2015;71:11–6.
[59] Jakubinek MB, Samarasekera CJ, White MA. Elephant ivory: a low thermal conductivity, high strength nanocomposite. J Mater Res 2006;21:287–92.
[60] Dugdale DS. Yielding of steel sheets containing slits. J Mech Phys Solids 1960;8:100–4.
[61] Burnett TL, Holroyd NH, Scamans GM, Zhou X, Thompson GE, Withers PJ. The role of crack branching in stress corrosion cracking of aluminium alloys. Corros Rev 2015;33:443–54.
[62] Weiss IM, Kirchner HO. Plasticity of two structural proteins: alpha-collagen and beta-keratin. J Mech Behav Biomed Mater 2011;4:733–43.
[63] Gupta HS, Fratzl P, Kerschnitzki M, Benecke G, Wagermaier W, Kirchner HO. Evidence for an elementary process in bone plasticity with an activation enthalpy of 1 eV. J R Soc Interface 2007;4:277–82.
[64] Gupta HS, Krauss S, Kerschnitzki M, Karunaratne A, Dunlop JWC, Barber AH, et al. Intrafibrillar plasticity through mineral/collagen sliding is the dominant mechanism for the extreme toughness of antler bone. J Mech Behav Biomed Mater 2013;28:366–82.
[65] Lees S. Considerations regarding the structure of the mammalian mineralized osteoid from viewpoint of the generalized packing model. Connect Tissue Res 1987;16:281–303.
[66] Saito H, Yokoi M. A 13C NMR study on collagens in the solid state: hydration/dehydration-induced conformational change of collagen and detection of internal motion. J Biochem 1992;111:376–82.
[67] Habelitz S, Balooch M, Marshall SJ, Balooch G, Marshall Jr GW. In situ atomic force microscopy of partially demineralized human dentin collagen fibrils. J Struct Biol 2002;138:227–36. Ecole doctorale Chimie physique et chimie analytique de Paris Centre (Paris).